

Letter

# Lens-Loaded Coded Aperture with Increased Information Capacity for Computational Microwave Imaging

Okan Yurduseven <sup>1,\*</sup>, Muhammad Ali Babar Abbasi <sup>1</sup> and Thomas Fromenteze <sup>2</sup>  
and Vincent Fusco <sup>1</sup>

<sup>1</sup> Institute of Electronics, Communications and Information Technology, Queen's University Belfast, Belfast BT3 9DT, UK; M.Abbasi@qub.ac.uk (M.A.B.A.); v.fusco@ecit.qub.ac.uk (V.F.)

<sup>2</sup> XLIM, University of Limoges, UMR 7252, F-87000 Limoges, France; thomas.fromenteze@unilim.fr

\* Correspondence: okan.yurduseven@qub.ac.uk

Received: 15 April 2020; Accepted: 7 May 2020; Published: 11 May 2020

**Abstract:** Computational imaging using coded apertures offers all-electronic operation with a substantially reduced hardware complexity for data acquisition. At the core of this technique is the single-pixel coded aperture modality, which produces spatio-temporally varying, quasi-random bases to encode the back-scattered radar data replacing the conventional pixel-by-pixel raster scanning requirement of conventional imaging techniques. For a frequency-diverse computational imaging radar, the coded aperture is of significant importance, governing key imaging metrics such as the orthogonality of the information encoded from the scene as the frequency is swept, and hence the conditioning of the imaging problem, directly impacting the fidelity of the reconstructed images. In this paper, we present dielectric lens loading of coded apertures as an effective way to increase the information coding capacity of frequency-diverse antennas for computational imaging problems. We show that by lens loading the coded aperture for the presented imaging problem, the number of *effective* measurement modes can be increased by 32% while the conditioning of the imaging problem is improved by a factor of greater than two times.

**Keywords:** microwaves; imaging; radar; metasurface; frequency-diversity; lens; singular value decomposition

## 1. Introduction

Imaging and sensing systems leveraging various microwave radar modalities have been the subject of much research with a variety of applications from remote sensing [1–8] to biomedical imaging [9–15] and security-screening [16–22] to name a few. This interest is justified by several advantages of electromagnetic (EM) waves at microwave frequencies, such as non-ionising radiation, their capability to operate in all-weather conditions and being able to penetrate through most optically opaque materials. A high level investigation of microwave imaging techniques presented in the literature reveals that most studies conducted in this area rely on mechanical or electronic raster scanning solutions. For example, in the case of synthetic aperture radar (SAR) based modalities, mechanical raster scanning the imaged scene is the predominantly adopted technique. In this technique, a composite aperture is synthesised using an antenna that is mechanically raster scanned at the Nyquist limit. Here, mechanical raster scanning suggests moving the antenna across multiple spatial sampling points separated by a distance of  $\lambda/2$ , where  $\lambda$  is the wavelength at the operating frequency. This approach relying on pixel-by-pixel raster scanning the imaged scene can substantially increase the data acquisition time, especially for applications requiring to synthesise electrically large apertures. An alternative solution to this is the use of the phased array approach, which can achieve the raster

scanning requirement in an all-electronic manner. Whereas the all-electronic operation of the phased array apertures can substantially improve the data acquisition speed, limitations to this technique persist. In this approach, each antenna element within the synthesised array aperture requires a dedicated phase shifting circuit to achieve a coherent phase response across the aperture to raster scan the radiation pattern of the array in an all-electronic manner. As a result, phased array radars, albeit exhibiting all-electronic operation, typically have a substantially complex hardware architecture and can consume a large amount of power.

Recently, an emerging concept, known as frequency-diverse computational imaging, has gained significant traction to address the challenges of the existing radar modalities [23–34]. Frequency-diverse imaging relies on a coded aperture principle. Using an aperture that radiates spatio-temporally varying field patterns as a function of a frequency-sweep is the key enabling technology behind the frequency-diverse computational imaging radar technique. In this modality, the spatio-temporally incoherent modes form a set of random bases to illuminate the imaged scene and collect the back-scattered measurements. Hence, at the heart of the frequency-diverse computational imaging technique is the idea to compress the back-scattered radar measurements using the transfer function of the coded apertures. Different from the conventional imaging modalities, this technique does not require raster scanning the scene due to the encoding of the scene information onto a set of quasi-random bases. Moreover, different from the SAR and phased array techniques requiring a number of channels equal to the number of sampling points (or antennas) within the synthesised composite aperture, the coded aperture compresses the back-scattered measurements into a single channel. This substantially reduces the complexity of the hardware layer. Therefore, the key component of the frequency-diverse computational imaging technique is the coded aperture. In the past, we have demonstrated several coded aperture modalities, such as cavity-backed metasurface antennas [28–30], printed planar metasurface antennas [31,32], and Mills-Cross shaped metasurface antennas [33,34]. Recently, the application of a Luneburg lens loaded 1D compressive device radiating a multi-beam azimuth radiation pattern controlled by the multiple input ports of the Luneburg lens has also been demonstrated as an interesting example [35]. A crucial aspect in governing the quality of the reconstructed images using our coded apertures [28–34], which can do 3D imaging with a single compressed channel, is the information capacity of the aperture used to encode the back-scattered measurements. A quantitative way to analyse the information capacity (and hence the orthogonality of the spatio-temporally incoherent measurement modes) of the coded aperture is to analyse the singular values of the imaging problem at hand. This can be achieved by doing a singular value decomposition (SVD) of the sensing matrix produced by the coded aperture [36,37]. In light of this, to improve the reconstruction quality of a computational frequency-diverse radar imaging system, it is vital that the singular value spectrum of the problem is optimised. In this work, we demonstrate the application of a lens-loaded frequency-diverse coded aperture as a way to increase the information coding capacity of coded apertures for computational imaging applications. We show, qualitatively (analysing reconstructed images) and quantitatively (analysing the singular values), that we can improve the conditioning of the imaging problem by loading the coded aperture with a lens. The outline of this paper is as follows: In Section 2, we provide a brief introduction to the frequency-diverse computational imaging technique. In Section 3, we demonstrate the concept of lens-loaded cavity-based metasurface antenna and its application to a near-field radar imaging problem. We present that the increased information capacity as a result of lens-loading the frequency-diverse antenna improves the quality of the reconstructed images. Finally, Section 4 provides the concluding remarks.

## 2. Methods

### 2.1. Frequency-Diverse Imaging Using Coded Apertures

Frequency-diverse imaging is a computational technique using spatially-varying quasi-random field patterns to illuminate the scene and capture the back-scattered signals from the scene as a

function of a frequency sweep. Using the first Born approximation, the first part of the imaging problem, known as the linearised forward-model, can be described in an integral form as follows:

$$g(r; w) = \int_{r'} E_{Tx}(r, r'; w) E_{Rx}(r, r'; w) f(r') dr' + n \quad (1)$$

In Equation (1),  $g$  denotes the measured back-scattered signal compressed by the transfer function of the coded aperture,  $E_{Tx}$  and  $E_{Rx}$  are the radiated electric field patterns from the transmit and receive apertures in the imaged scene ( $E_{Tx} = E_{Rx}$  if the same aperture is used, i.e., monostatic layout as adopted in this work),  $f$  is the susceptibility distribution of the scene to be imaged,  $n$  is the system noise,  $w$  is the frequency, and  $r(x, y, z)$  and  $r(x', y', z')$  denote the aperture and scene coordinates, respectively. Discretising the integral equation of Equation (1), there are two important parameters in the definition of the discrete forward-model, namely the number of measurement modes,  $M$ , and the number of voxels in the scene,  $N$ :

$$\mathbf{g}_{M \times 1} = \mathbf{H}_{M \times N} \mathbf{f}_{N \times 1} + \mathbf{n}_{M \times 1} \quad (2)$$

In Equation (2), we consider scalar fields and use the bold font to denote the vector-matrix notation. The number of measurement modes can be calculated as  $M = \text{Number of transmit antennas} \times \text{number of receive antennas} \times \text{number of frequency sampling points}$ . Hence, the sensing matrix (or the coded aperture transfer function),  $\mathbf{H}$ , linking the imaged scene to the compressed measurements is of the size  $M \times N$ . Under the first Born approximation, the sensing matrix  $\mathbf{H}$  can be linked to the radiated electric field patterns from the transmit and receive coded apertures propagated to the imaged scene as  $\mathbf{H} \propto E_{Tx} E_{Rx}$  [24]. It is evident from this description that the sensing matrix is a fat matrix (not necessarily a square matrix,  $M \neq N$ ), therefore, does not have an exact inverse. Retrieving the scene information from the compressed measurements is an inverse problem. From the discretised forward-model of Equation (2), recovering an estimate of the scene information,  $f_{est}$ , can be achieved by means of an adjoint operation, relying on a single-shot phase compensation as follows:

$$\mathbf{f}_{est} = \mathbf{H}^\dagger \mathbf{g} \quad (3)$$

In Equation (3), symbol  $\dagger$  denotes the conjugate-transpose operation, suggesting that the phase conjugated sensing matrix is applied to the compressed signal to retrieve an estimate of the scene information. This technique is known as matched-filtering and can be adopted as a rather simple reconstruction algorithm in frequency-diverse computational imaging problems.

## 2.2. Information Capacity Metrics

From the forward-model of the imaging problem, it is evident that the sensing matrix contains all the information that we need to characterize the orthogonality of the field patterns radiated by frequency-diverse antennas. A particularly useful metric in the analysis of this figure of merit is the SVD of the sensing matrix:

$$\mathbf{H}_{M \times N} = \mathbf{U}_{M \times M} \boldsymbol{\sigma}_{M \times N} \mathbf{V}_{N \times N}^T \quad (4)$$

In Equation (4),  $\boldsymbol{\sigma}$  is a diagonal matrix with the diagonal axis of this matrix revealing the singular values in a descending order. Therefore, plotting these singular values gives us an insight into how flat the singular value spectrum is. A particularly useful metric from this observation is the number of *effective* measurement modes for a given signal-to-noise (SNR) level, corresponding to the number of measurement modes that remain above the noise level [36]. The addition of noise to the measured back-scattered signal is achieved by using a zero mean Gaussian distribution with a variance proportional to the selected SNR level [36]. The SVD analysis also produces an important parameter known as the condition number for the inverse problem that can directly be calculated from the singular value pattern as [37]:

$$CN = \sigma_{max} / \sigma_{min} \quad (5)$$

From Equation (5), it is evident that improving the condition number of the imaging problem can be achieved by flattening (reducing the decay slope) the singular value pattern. In the next section, we show that by lens loading a frequency-diverse antenna, the number of effective measurement modes, the condition number of the imaging problem, and hence the quality of the reconstructed images, can be improved.

### 3. Results and Discussion

The studied frequency-diverse computational imaging system consists of a single cavity-backed metasurface antenna operating in a monostatic transceiver mode, as depicted in Figure 1.

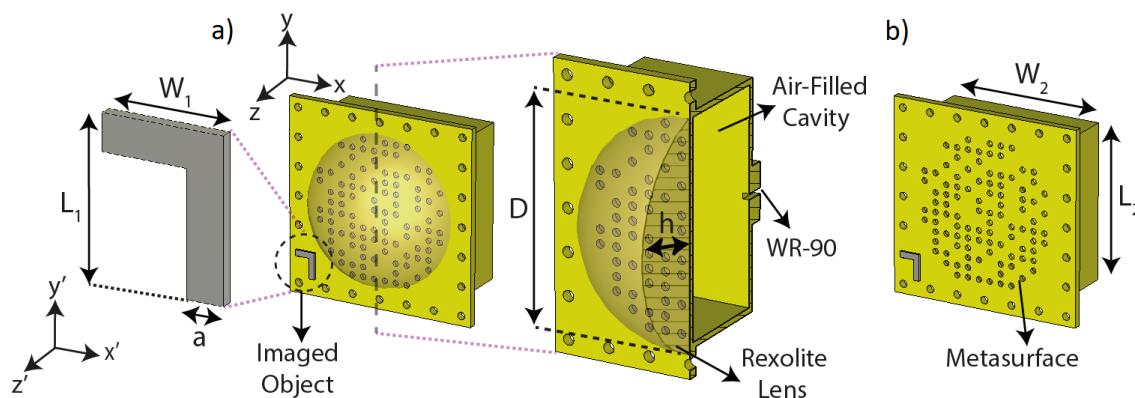


**Figure 1.** Depiction of the studied imaging scenario (a) frequency-diverse computational imaging of an L-shaped phantom with lens (b) frequency-diverse computational imaging of an L-shaped phantom without lens. Dimensions:  $L_1 = 5$  cm,  $W_1 = 5$  cm,  $L_2 = 0.4$  m,  $W_2 = 0.4$  m,  $D = 0.4$  m,  $h = 0.15$  m,  $a = 1.5$  cm. Aperture coordinates are  $r(x, y, z)$  and scene coordinates are  $r'(x', y', z')$ .

As shown in Figure 1, the back-scattered signal from the scene is compressed into the transceiver channel (WR-90 waveguide port) of the frequency-diverse antenna. The antenna has a size of  $0.4 \text{ m} \times 0.4 \text{ m}$  in the transverse-plane ( $xy$ -plane). The aperture of the frequency-diverse antenna is loaded with a semi-spherical shaped dielectric lens. The lens material is selected to be Rexolite with  $\epsilon_r = 2.53$  and  $\tan\delta = 0.0001$  [38,39]. For practical applications, Rexolite material is known for its rigidity and low-loss characteristics, making it a suitable material choice for the lens design. Using the depicted computational imaging system scenario in Figure 1, we image an L-shaped phantom placed within the near-field of the lens-loaded frequency-diverse antenna at a distance of  $d = 0.35$  m. As depicted in Figure 1, the size of the L-shaped phantom is  $5 \times 5$  cm. For the studied imaging scenario, the L-shaped phantom is modelled as a metal scatter with the reflectivity of the phantom set to 1 while the rest of the scene has a reflectivity of 0. It should be mentioned that the frequency-diverse imaging technique can also deal with objects with spatially varying reflectivity values. An important point can be made about the frequency dependence of the defined susceptibility distribution for the imaged object. We note that due to the small frequency bandwidth of operation, 2 GHz, this variation is negligible. This assumption is widely adopted by the microwave and millimetre-wave imaging communities, even with substantially larger operating bandwidths [18,34,40]. For the imaging frequency, we choose the 9–11 GHz band within the X-band frequency regime (8–12 GHz). The operating frequency-band is sampled at 201 frequency sampling points with the stepping frequency selected to be  $\Delta_f = 10$  MHz. Using these imaging metrics, from well-known diffraction limited standard radar resolution equations [36], the theoretical cross-range ( $xy$ -plane) resolution limit at the maximum frequency, 11 GHz, is  $\delta_{cr} \approx 1.8$  cm. Therefore, we choose the width of the vertical and horizontal metal strips forming the L-shaped phantom to be 1.5 cm, in accordance with the cross-range resolution limit of the aperture. For the imaging framework, the transfer function of the lens-loaded metasurface antenna is simulated using a full-wave solver, CST Microwave Studio. The characterisation data (near-field electric field distribution) is then imported into our numerical

model in MATLAB for imaging. The characterisation step of the metasurface antenna is performed twice, with and without the lens, and each near-field data is stored separately to compare the imaging characteristics. From full-wave simulations, the simulated reflection coefficient,  $S_{11}$ , data is shown in Figure 2 whereas the near-field electric field patterns radiated by the lens-loaded frequency-diverse metasurface antenna are shown in Figure 3. As can be seen in Figure 2, the lens-loaded metasurface antenna exhibits a good impedance match response with the  $|S_{11}|$  level remaining around or below  $-10$  dB across the operating frequency band. The presence of multiple cavity modes is evident from the multiple resonance behaviour of the  $S_{11}$  pattern across 9–11 GHz, which is also evidenced by the diversity of the radiated electric field patterns shown at around 10 GHz in Figure 3.

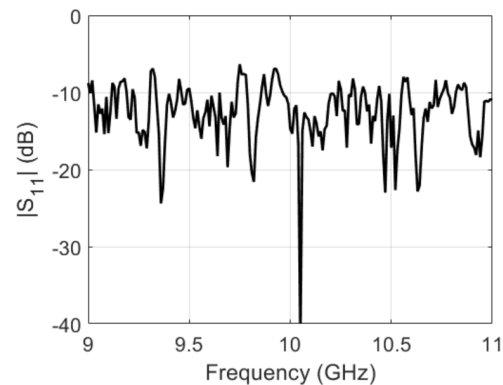


**Figure 2.** Simulated reflection coefficient pattern of the lens-loaded frequency-diverse metasurface antenna.

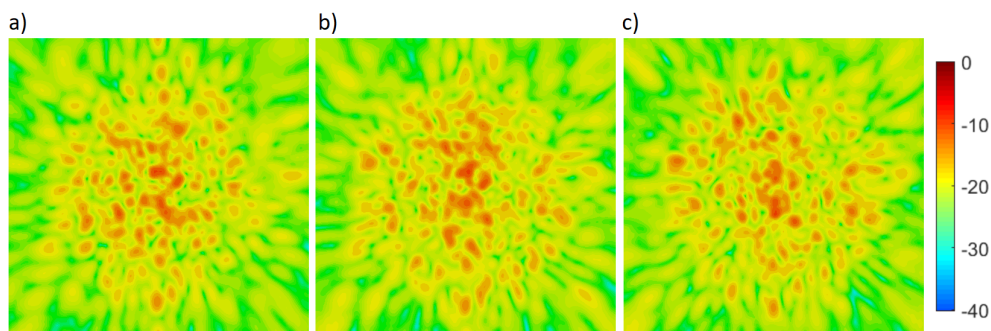


**Figure 3.** Characterised near-field electric field data at adjacent frequencies: (a) 9.99 GHz (b) 10 GHz (c) 10.01 GHz. Colorbar in dB.

The reconstructed image of the L-shaped phantom with and without the lens-loaded metasurface antenna is shown in Figure 4. Comparing the images in Figure 4, the fidelity of the image reconstructed using the lens-loaded metasurface antenna (Figure 4b) is superior in comparison to the image reconstructed using the cavity-backed metasurface antenna without the lens (Figure 4a). Both images are plotted on the same dynamic range, 20 dB, and whereas the image reconstructed using the lens-loaded frequency-diverse system reveals a full outline of the imaged phantom, the image reconstructed using the unloaded metasurface antenna reveals rather limited information about the object. Because the presented technique performs 3D imaging, in Figure 4d, we also present the depth profile of the reconstructed image with the lens-loaded layout. From Figure 4d, the imaged object appears at the intended depth  $d = 0.35$  m. The extent of the imaged phantom in the  $yz$ -plane fills a depth slot with a width of around 6.5 cm, which is in good agreement with the calculated theoretical depth resolution with a 2 GHz imaging bandwidth, 7.5 cm, using the standard radar range resolution equation [36]. The improvement in the obtained range profile in comparison to the theoretical limit is due near-field operation, which improves the range resolution beyond the traditional far-field limit [41]. To provide a comparison between the reflectivity profile of the original L-shaped phantom (ground truth in Figure 4c) and the reconstructed reflectivity distribution, in Figure 4b, we take a

slice along  $y = 0$  m and plot the ground truth and reconstructed reflectivity values along this axis. As can be seen in Figure 4e, the reconstructed reflectivity profile exhibits a good agreement with the ground truth reflectivity envelope. The spatial spreading in the reconstructed reflectivity profile is due to the diffraction limited resolution of the computational imaging system. An analysis of the spatial Fourier domain ( $k$ -space) representation of the radiated electric field data from the lens-loaded metasurface antenna in Figure 5 demonstrates the effect of lens loading the antenna. Whereas at individual frequency sampling points (shown for only 9 GHz in Figure 5a and 11 GHz in Figure 5b for the sake of clarity), we sample varying sets of  $k$ -vectors, an incoherent (intensity) based summation of the spatial Fourier transformed radiated electric-field data over 201 frequency points exhibits a plane-wave representation in the broadside direction of the coded aperture. This suggests that, in the scene spatial domain,  $r'(x', y', z')$ , we provide a sufficient illumination of the object when all the sampling frequency points are combined.

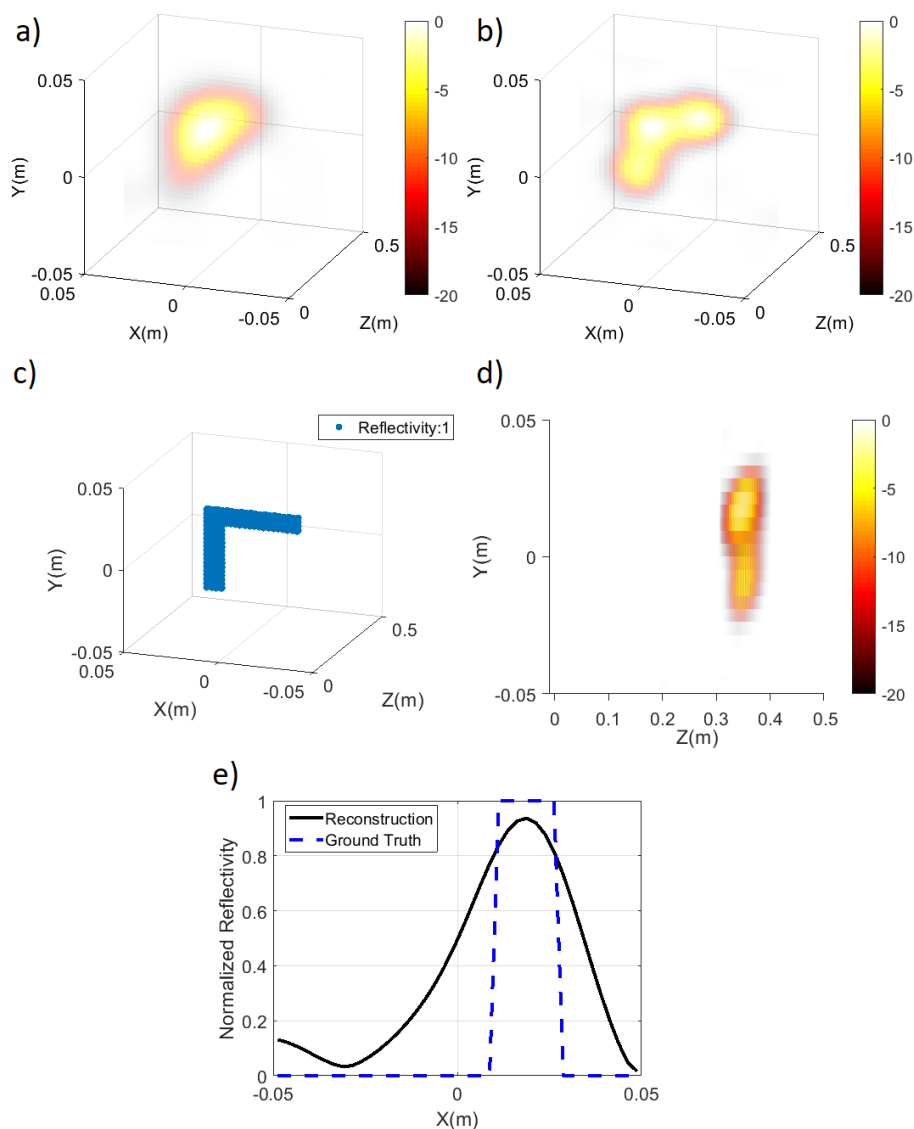


**Figure 4.** Reconstructed images of an L-shaped gun phantom, (a) reconstructed microwave image without the lens-loaded metasurface antenna, (b) reconstructed image with the lens-loaded metasurface antenna, (c) reflectivity distribution of the imaged scene (ground truth), (d) reconstructed image of the gun phantom in the  $yz$ -plane (depth), (e) reflectivity distribution comparison between the ground truth and the reconstructed image along  $y = 0$  m slice. Colorbar is in dB scale.

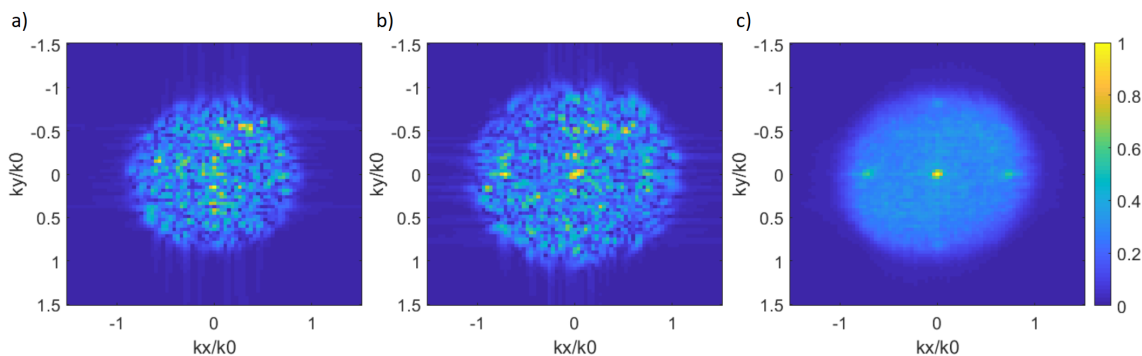


**Figure 5.** Normalised spatial frequency domain (k-space) representation of the coded aperture radiated fields, (a) 9 GHz, (b) 11 GHz, (c) overall k-space pattern formed by incoherent superposition (summing up intensity data) of the k-transformed coded aperture radiated fields for 201 frequency points.

This qualitative assessment and the improvement in the reconstructed image can be further supported from a quantitative point of view by investigating the singular value spectrum of the studied imaging problem. A comparison between the singular value patterns with and without lens-loading the metasurface antenna is shown in Figure 6.

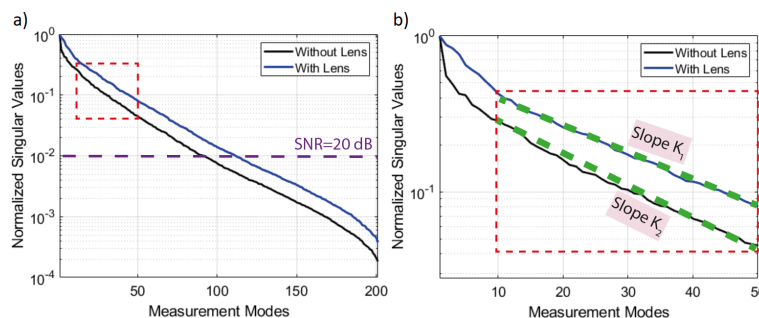


**Figure 6.** Comparison of the SVD patterns with and without the loaded lens, (a) SVD spectrum for the entire 201 measurement modes. The system SNR level is highlighted in the same SVD plot to provide a reference threshold for the effective number of measurement modes, (b) zoomed in SVD window with significant singular value components remaining above the 20 dB SNR level. The selected region exhibits a rather linear decay spectrum with the decay slope labelled  $K_1$  (with lens) and  $K_2$  (without lens), respectively.  $K_1 = 0.8K_2$  within the highlighted window.

As can be seen in Figure 6, the SVD pattern extracted from the sensing matrix of the lens-loaded cavity-backed metasurface antenna exhibits a slower decay response in comparison to the SVD pattern of the unloaded cavity-backed metasurface antenna. This behaviour is especially evident for the most significant singular value components remaining above the 20 dB SNR level selected for the studied imaging scenario. Defining a small window above the SNR = 20 dB region and doing a linear regression analysis within the selected window of measurement modes from  $M = 10$  to  $M = 50$ , where the decay profile is rather linear, as shown in Figure 4b, we find that the singular value of the imaging problem drops from  $\sigma = 0.42$  to  $\sigma = 0.081$ , or by a factor of 5.2 times with the lens. Without the lens, the singular value of the imaging problem within the same window drops from  $\sigma = 0.29$  to  $\sigma = 0.045$ , or by a factor of 6.5 times. Hence, comparing the slope of the SVD curves within the selected window ( $K_1$  with the lens and  $K_2$  without the lens, as highlighted in Figure 4b), we have  $K_1 = 0.8K_2$ . We note that because both SVD patterns exhibit a fairly linear decay profile after the selected window, the calculated decay slopes are also accurate going beyond the 20 dB SNR level. The slower decay of the SVD pattern suggests that the orthogonality of the measurement modes produced by the lens-loaded metasurface antenna is higher. This in turn suggests that the redundancy of the gathered scene information that is mapped out by each mode is lower, corresponding to an increased information capacity encoded by the metasurface antenna. To put this statement into context, from Figure 6a,

we can calculate the number of effective measurement modes that remain above the selected SNR level for the studied imaging scenario, 20 dB. From Figure 6a, it can be seen that, for SNR = 20 dB, the number of effective measurement modes is 115 for the frequency-diverse computational radar loaded with the lens whereas without the lens, the number of effective measurement modes drops to 87. This suggests that the lens-loaded cavity-backed metasurface antenna exhibits 32% higher number of useful measurement modes. Another important figure of merit for the studied inverse problem is the condition number of the singular values. By taking the number of effective measurement modes with the lens-loaded configuration (115) as a reference to determine the smallest singular value for both cases, from Equation (5), the imaging condition number is calculated to be  $CN_{LENS} = \frac{\sigma_{max} = 1}{\sigma_{min} = 0.01} = 100$  for the lens-loaded configuration and  $CN_{NO-LENS} = \frac{\sigma_{max} = 1}{\sigma_{min} = 0.0045} = 222$  without the lens. This suggests that lens loading the metasurface antenna improves the conditioning of the imaging problem by a factor of more than 50%.

#### 4. Conclusions

In this paper, we have presented a lens-loading technique to increase the orthogonality of the measurement modes radiated by a frequency-diverse cavity-backed metasurface antenna at X-band frequencies. It has been shown that the image reconstructed using the lens-loaded cavity exhibits a substantially improved fidelity in comparison to the image reconstructed without the lens. To quantitatively analyse the underlying reason behind this improvement, we have studied the singular value spectrum of the considered imaging problem and showed that the lens loading of the metasurface antenna flattens the SVD spectrum, reducing the amount of correlation between the information encoded at adjacent frequency points within the selected operating frequency band. A further analysis of this observation has revealed that lens loading the metasurface antenna has increased the number of effective measurement modes remaining above the imaging SNR level from 87 to 115, while more than halving the imaging condition number. We note that the proposed technique is not specific to a particular reconstruction technique and although matched-filtering has been adopted as the computational imaging reconstruction algorithm, the benefit of improved number of useful measurement modes and SVD response can be even more dominant when other reconstruction techniques are applied, such as pseudo-inversion, which is more susceptible to poor singular values than the matched-filtering algorithm. In general, the accuracy of the frequency-diverse imaging technique is heavily governed by the phase calibration precision of the sensing matrix [34,42] and we note that such constraints can be substantially simplified using phaseless reconstruction algorithms [43,44]. Although demonstrated at X-band frequencies and for near-field radar imaging, the presented technique can be adopted in a plethora of applications, from remote sensing to direction of arrival estimation [45], and can readily be scaled to different frequency bands, such as millimetre-wave band and above.

**Author Contributions:** Conceptualisation, O.Y., M.A.B.A.; methodology, O.Y., T.F.; software, O.Y.; validation, O.Y.; formal analysis, O.Y.; investigation, O.Y., M.A.B.A., T.F., V.F.; data curation, O.Y.; writing—original draft preparation, O.Y.; writing—review and editing, O.Y., M.A.B.A., T.F., V.F.; visualisation, O.Y.; supervision, O.Y.; project administration, O.Y.; funding acquisition, O.Y. All authors have read and agreed to the submitted version of the manuscript.

**Funding:** This work was funded by the Leverhulme Trust under Research Leadership Award RL-2019-019. The work of V.F. was supported by the UK Engineering and Physical Sciences Research Council (EPSRC) EP/N020391/1.

**Conflicts of Interest:** The authors declare no conflict of interest.

## References

1. Montzka, C.; Jagdhuber, T.; Horn, R.; Bogena, H.R.; Hajnsek, I.; Reigber, A.; Vereecken, H. Investigation of SMAP fusion algorithms with airborne active and passive L-band microwave remote sensing. *IEEE Trans. Geosci. Remote Sens.* **2016**, *54*, 3878–3889. [[CrossRef](#)]
2. Gharechelou, S.; Tateishi, R.; A Johnson, B. A Simple Method for the Parameterization of Surface Roughness from Microwave Remote Sensing. *Remote Sens.* **2018**, *10*, 1711. [[CrossRef](#)]
3. Jonard, F.; Bircher, S.; Demontoux, F.; Weihermüller, L.; Razafindratsima, S.; Wigneron, J.P.; Vereecken, H. Passive L-band microwave remote sensing of organic soil surface layers: A tower-based experiment. *Remote Sens.* **2018**, *10*, 304. [[CrossRef](#)]
4. Kim, Y.; Jackson, T.; Bindlish, R.; Lee, H.; Hong, S. Radar vegetation index for estimating the vegetation water content of rice and soybean. *IEEE Geosci. Remote Sens. Lett.* **2011**, *9*, 564–568.
5. Das, K.; Paul, P.K. Present status of soil moisture estimation by microwave remote sensing. *Cogent Geosci.* **2015**, *1*, 1084669. [[CrossRef](#)]
6. Hwang, P.A.; Fois, F. Surface roughness and breaking wave properties retrieved from polarimetric microwave radar backscattering. *J. Geophys. Res. Ocean.* **2015**, *120*, 3640–3657. [[CrossRef](#)]
7. Wang, W.Q.; Cai, J.; Peng, Q. Near-space microwave radar remote sensing: Potentials and challenge analysis. *Remote Sens.* **2010**, *2*, 717–739. [[CrossRef](#)]
8. Kim, Y.; Reck, T.J.; Alonso-delPino, M.; Painter, T.H.; Marshall, H.P.; Bair, E.H.; Dozier, J.; Chattopadhyay, G.; Liou, K.N.; Chang, M.C.F.; et al. A Ku-Band CMOS FMCW Radar Transceiver for Snowpack Remote Sensing. *IEEE Trans. Microw. Theory Tech.* **2018**, *66*, 2480–2494. [[CrossRef](#)]
9. Nikolova, N.K. Microwave imaging for breast cancer. *IEEE Microw. Mag.* **2011**, *12*, 78–94. [[CrossRef](#)]
10. Bourqui, J.; Sill, J.M.; Fear, E.C. A prototype system for measuring microwave frequency reflections from the breast. *Int. J. Biomed. Imaging* **2012**, 2012. [[CrossRef](#)]
11. Porter, E.; Coates, M.; Popović, M. An early clinical study of time-domain microwave radar for breast health monitoring. *IEEE Trans. Biomed. Eng.* **2015**, *63*, 530–539. [[CrossRef](#)] [[PubMed](#)]
12. Byrne, D.; Craddock, I.J. Time-domain wideband adaptive beamforming for radar breast imaging. *IEEE Trans. Antennas Propag.* **2015**, *63*, 1725–1735. [[CrossRef](#)]
13. Kwon, S.; Lee, S. Recent advances in microwave imaging for breast cancer detection. *Int. J. Biomed. Imaging* **2016**, 2016. [[CrossRef](#)] [[PubMed](#)]
14. Elsdon, M.; Yurduseven, O.; Smith, D. Early stage breast cancer detection using indirect microwave holography. *Prog. Electromagn. Res.* **2013**, *143*, 405–419. [[CrossRef](#)]
15. Abbak, M.; Cayoren, M.; Akduman, I. Microwave breast phantom measurements with a cavity-backed Vivaldi antenna. *IET Microw. Antennas Propag.* **2014**, *8*, 1127–1133. [[CrossRef](#)]
16. Gonzalez-Valdes, B.; Alvarez, Y.; Mantzavinos, S.; Rappaport, C.M.; Las-Heras, F.; Martinez-Lorenzo, J.A. Improving security screening: A comparison of multistatic radar configurations for human body imaging. *IEEE Antennas Propag. Mag.* **2016**, *58*, 35–47. [[CrossRef](#)]
17. Blackhurst, E.; Salmon, N.; Southgate, M. Full polarimetric millimetre wave radar for stand-off security screening. In *Millimetre Wave and Terahertz Sensors and Technology X*; International Society for Optics and Photonics: 2017; Volume 10439, p. 1043906.
18. Sheen, D.M.; McMakin, D.L.; Hall, T.E. Three-dimensional millimeter-wave imaging for concealed weapon detection. *IEEE Trans. Microw. Theory Tech.* **2001**, *49*, 1581–1592. [[CrossRef](#)]
19. Yurduseven, O. Indirect microwave holographic imaging of concealed ordnance for airport security imaging systems. *Prog. Electromagn. Res.* **2014**, *146*, 7–13. [[CrossRef](#)]
20. Zhuge, X.; Yarovoy, A.G. A sparse aperture MIMO-SAR-based UWB imaging system for concealed weapon detection. *IEEE Trans. Geosci. Remote Sens.* **2010**, *49*, 509–518. [[CrossRef](#)]
21. Crocco, L. Detection of Concealed Targets in Through-the-Wall Imaging. In *Through-the-Wall Radar Imaging*; CRC Press: Boca Raton, FL, USA, 2017; pp. 449–470.
22. Marks, D.L.; Yurduseven, O.; Smith, D.R. Sparse blind deconvolution for imaging through layered media. *Optica* **2017**, *4*, 1514–1521. [[CrossRef](#)]
23. Hunt, J.; Driscoll, T.; Mrozack, A.; Lipworth, G.; Reynolds, M.; Brady, D.; Smith, D.R. Metamaterial apertures for computational imaging. *Science* **2013**, *339*, 310–313. [[CrossRef](#)] [[PubMed](#)]

24. Lipworth, G.; Mrozack, A.; Hunt, J.; Marks, D.L.; Driscoll, T.; Brady, D.; Smith, D.R. Metamaterial apertures for coherent computational imaging on the physical layer. *JOSA A* **2013**, *30*, 1603–1612. [[CrossRef](#)] [[PubMed](#)]
25. Wu, Z.; Zhang, L.; Liu, H.; Kou, N. Range decoupling algorithm for accelerating metamaterial apertures-based computational imaging. *IEEE Sens. J.* **2018**, *18*, 3619–3631. [[CrossRef](#)]
26. Zvolensky, T.; Gollub, J.N.; Marks, D.L.; Smith, D.R. Design and analysis of a W-band metasurface-based computational imaging system. *IEEE Access* **2017**, *5*, 9911–9918. [[CrossRef](#)]
27. Zhu, S.; Zhao, M.; Dong, X.; Shi, H.; Lu, R.; Chen, X.; Zhang, A. Differential coincidence imaging with frequency diverse aperture. *IEEE Antennas Wirel. Propag. Lett.* **2018**, *17*, 964–968. [[CrossRef](#)]
28. Marks, D.L.; Yurduseven, O.; Smith, D.R. Cavity-backed metasurface antennas and their application to frequency diversity imaging. *JOSA A* **2017**, *34*, 472–480. [[CrossRef](#)]
29. Yurduseven, O.; Flowers, P.; Ye, S.; Marks, D.L.; Gollub, J.N.; Fromenteze, T.; Wiley, B.J.; Smith, D.R. Computational microwave imaging using 3D printed conductive polymer frequency-diverse metasurface antennas. *IET Microw. Antennas Propag.* **2017**, *11*, 1962–1969. [[CrossRef](#)]
30. Fromenteze, T.; Yurduseven, O.; Imani, M.F.; Gollub, J.; Decroze, C.; Carsenat, D.; Smith, D.R. Computational imaging using a mode-mixing cavity at microwave frequencies. *Appl. Phys. Lett.* **2015**, *106*, 194104. [[CrossRef](#)]
31. Yurduseven, O.; Gowda, V.R.; Gollub, J.N.; Smith, D.R. Printed aperiodic cavity for computational and microwave imaging. *IEEE Microw. Wirel. Compon. Lett.* **2016**, *26*, 367–369. [[CrossRef](#)]
32. Yurduseven, O.; Gowda, V.R.; Gollub, J.N.; Smith, D.R. Multistatic microwave imaging with arrays of planar cavities. *IET Microw. Antennas Propag.* **2016**, *10*, 1174–1181. [[CrossRef](#)]
33. Yurduseven, O.; Gollub, J.N.; Marks, D.L.; Smith, D.R. Frequency-diverse microwave imaging using planar Mills-Cross cavity apertures. *Opt. Express* **2016**, *24*, 8907–8925. [[CrossRef](#)] [[PubMed](#)]
34. Gollub, J.; Yurduseven, O.; Trofatter, K.; Arnitz, D.; Imani, M.; Sleasman, T.; Boyarsky, M.; Rose, A.; Pedross-Engel, A.; Odabasi, H.; et al. Large metasurface aperture for millimeter wave computational imaging at the human-scale. *Sci. Rep.* **2017**, *7*, 42650. [[CrossRef](#)] [[PubMed](#)]
35. Jouade, A.; Meric, S.; Lafond, O.; Himdi, M.; Ferro-Famil, L. A passive compressive device associated with a lüneburg lens for multibeam radar at millimeter wave. *IEEE Antennas Wirel. Propag. Lett.* **2018**, *17*, 938–941. [[CrossRef](#)]
36. Yurduseven, O.; Imani, M.F.; Odabasi, H.; Gollub, J.; Lipworth, G.; Rose, A.; Smith, D.R. Resolution of the frequency diverse metamaterial aperture imager. *Prog. Electromagn. Res.* **2015**, *150*, 97–107. [[CrossRef](#)]
37. Fromenteze, T.; Kpré, E.L.; Carsenat, D.; Decroze, C.; Sakamoto, T. Single-shot compressive multiple-inputs multiple-outputs radar imaging using a two-port passive device. *IEEE Access* **2016**, *4*, 1050–1060. [[CrossRef](#)]
38. Abbasi, M.A.B.; Fusco, V.F.; Tataria, H.; Matthaiou, M. Constant- $\epsilon_r$  Lens Beamformer for Low-Complexity Millimeter-Wave Hybrid MIMO. *IEEE Trans. Microw. Theory Tech.* **2019**, *67*, 2894–2903. [[CrossRef](#)]
39. Yurduseven, O.; Abbasi, M.A.B.; Fusco, V. Lens Antenna and Systems Incorporating Same. UK Patent No. 2004233.9, 2020 (filed).
40. Ahmed, S.S.; Schiessl, A.; Schmidt, L.P. A novel fully electronic active real-time imager based on a planar multistatic sparse array. *IEEE Trans. Microw. Theory Tech.* **2011**, *59*, 3567–3576. [[CrossRef](#)]
41. Sleasman, T.; Boyarsky, M.; Imani, M.F.; Fromenteze, T.; Gollub, J.N.; Smith, D.R. Single-frequency microwave imaging with dynamic metasurface apertures. *JOSA B* **2017**, *34*, 1713–1726. [[CrossRef](#)]
42. Yurduseven, O.; Gollub, J.N.; Trofatter, K.P.; Marks, D.L.; Rose, A.; Smith, D.R. Software calibration of a frequency-diverse, multistatic, computational imaging system. *IEEE Access* **2016**, *4*, 2488–2497. [[CrossRef](#)]
43. Yurduseven, O.; Fromenteze, T.; Smith, D.R. Relaxation of alignment errors and phase calibration in computational frequency-diverse imaging using phase retrieval. *IEEE Access* **2018**, *6*, 14884–14894. [[CrossRef](#)]
44. Fromenteze, T.; Liu, X.; Boyarsky, M.; Gollub, J.; Smith, D.R. Phaseless computational imaging with a radiating metasurface. *Opt. Express* **2016**, *24*, 16760–16776. [[CrossRef](#)] [[PubMed](#)]
45. Yurduseven, O.; Abbasi, M.A.B.; Fromenteze, T.; Fusco, V. Frequency-Diverse Computational Direction of Arrival Estimation Technique. *Sci. Rep.* **2019**, *9*, 1–12. [[CrossRef](#)] [[PubMed](#)]

